CrossMark

JfM PAPERS

Equilibrium shapes and floatability of static and vertically vibrated heavy liquid drops on the surface of a lighter fluid

Andrey Pototsky[1],†, Alexander Oron[2] and Michael Bestehorn[3]

[1]Department of Mathematics, Swinburne University of Technology, Hawthorn, Victoria 3122, Australia

[2]Department of Mechanical Engineering, Technion-Israel Institute of Technology, Haifa 3200003, Israel

[3]Institute of Physics, Brandenburg University of Technology, 03013 Cottbus-Senftenberg, Germany

A small drop of a heavier fluid may float on the surface of a lighter fluid supported by surface tension forces. In equilibrium, the drop assumes a radially symmetric shape with a circular triple-phase contact line. We show that such a floating liquid drop with a sufficiently small volume has two distinct equilibrium shapes at terrestrial gravity: one with a larger and one with a smaller radius of the triple-phase contact line. Static stability analysis reveals that both shapes could be stable if the drop volume is below a certain critical value. Experiments conducted with µL-sized water drops floating on commercial oil support the existence of multiple contact line radii for a drop with fixed volume. Next, we experimentally study the floatability of a less viscous water drop on the surface of a more viscous and less dense oil, subjected to a low-frequency (Hz-order) vertical vibration. We find that in a certain range of amplitudes, vibration helps heavy liquid drops to stay afloat. The physical mechanism of the increased floatability is explained by the horizontal elongation of the drop driven by subharmonic Faraday waves. The average length of the triple-phase contact line increases as the drop elongates that leads to a larger average lifting force produced by the surface tension.

Key words: drops, Faraday waves

1. Introduction

Floatation of a small liquid droplet on the surface of a less dense carrier fluid is a striking manifestation of the strength of tensile forces that exist between immiscible liquid and gaseous phases. When in equilibrium, the drop assumes a radially symmetric shape with a circular triple-phase contact line that separates the drop into a sessile upper cap and a pendant lower part. The quintessential question of determining the largest possible drop volume capable of staying afloat was first formulated and studied over 40 years ago

† Email address for correspondence: apototskyy@swin.edu.au

(Hartland & Burri 1976). From the theoretical point of view, the stationary shape of a liquid drop can be found by solving the minimal surface problem for liquid menisci, subject to a zero net force condition acting on the triple-phase contact line (Princen 1963; Princen & Mason 1965). Owing to its nonlinear nature and complexity of the boundary conditions, this problem can only be approached numerically for a particular combination of fluids. Prior to the modern era of personal computers, the computation of stationary drop shapes was a highly tedious task that involved manual manipulation of the tabulated solutions of the minimal surface equations. This method was used by Hartland & Burri (1976) to determine the maximum possible drop volume as a function of the fluid densities and interfacial tensions. Extending the original work of Hartland & Burri (1976), subsequent studies focused on experimental verification of the floatability of water drops on oil surfaces (Phan *et al.* 2012; Phan 2014), the floatability of non-wetting and Leidenfrost drops and liquid marbles (Ooi *et al.* 2016; Wong, Adda-Bedia & Vella 2017), addressing the role of the line tension (Bratukhin, Makarov & Teplova 2001; George *et al.* 2016) and developing a simplified model by assuming that the upper sessile cap of the drop is approximately flat (Bratukhin & Makarov 1994).

Here we use the numerical continuation method and conduct a series of experiments to reveal a previously unreported multistability of sufficiently small liquid drops floating on the surface of a less dense bulk fluid. Depending on the deposition method, a small quantity of a heavy fluid may form a floating drop with two different equilibrium radially symmetric shapes: one with a smaller and one with a larger radius of the triple-phase contact line. It should be emphasized that the existence of two different equilibrium shapes with a fixed drop volume was first mentioned by Hartland & Burri (1976), but the shape with the smaller value of the contact radius was discarded as being unstable. We conduct a static stability analysis of a floating drop and show that below a certain critical volume, both equilibrium shapes could be stable at terrestrial gravity. Our findings are supported by experimental observation of μL-sized water drops floating on the surface of a commercial oil. Thus we find that a 5 ± 1 μL water drop may form a triple-phase contact line with a variable radius, depending on the method of its deposition onto the oil surface. Transition from the smaller contact radius to the larger contact radius configuration is demonstrated by applying a gentle mechanical perturbation to the upper part of the floating water drop.

Our next goal is to experimentally study the dynamic floatability of a vertically vibrated water drop on the surface of a more viscous and less dense oil bath. In contrast to its anticipated destructive effect, external vibration is known to suppress the Rayleigh–Taylor instability in stratified liquid films and in liquid films on the underside of a solid plate (Wolf 1969, 1970; Lapuerta, Mancebo & Vega 2001; Bestehorn & Pototsky 2016; Pototsky & Bestehorn 2016; Sterman-Cohen, Bestehorn & Oron 2017). In a series of recent experiments, vertical shaking was shown to create levitating layers of a heavy fluid up to 20 cm in width floating on top of a lighter fluid (Apffel *et al.* 2015). A rather remarkable phenomenon of the upside-down floatability was revealed, when a solid body positioned at the lower interface of a levitating layer acquired a stable buoyancy position under the action of vertical vibration (Apffel *et al.* 2015).

Earlier, we developed a long-wave hydrodynamic model to investigate the saturation of the Rayleigh–Taylor instability in isolated vertically vibrated two-dimensional liquid drops on the surface of a finite-thickness carrier liquid film (Pototsky, Oron & Bestehorn 2019). In the absence of vibration, a small quantity of a heavy fluid, deposited on the surface of a less dense carrier film, stretches into a liquid column. The tip of the extending column eventually reaches the solid substrate and the carrier film ruptures. We have shown that an external vertical vibration prevents film rupture at non-zero Reynolds numbers, which leads to the formation of a stable floating drop.

Motivated by these findings, we conduct here a series of experiments with water drops on a vibrated oil surface and demonstrate that in a certain range of the vibration amplitudes and frequencies, the floatability of the drop is enhanced, which allows a larger quantity of water to stay afloat. In this regime, the drop elongates horizontally driven by the subharmonic surface Faraday waves that develop in its upper sessile cap (Pucci *et al.* 2011; Pucci, Ben Amar & Couder 2013). The time-averaged total length of the triple-phase contact line increases for the elongated drop, which leads to a larger lifting force generated by tensile forces. This new dynamical regime exists in a narrow window of the vibration amplitudes: above the onset of the Faraday waves in the drop and below the onset of the Faraday waves on the more viscous oil surface. An even stronger vibration destroys the balance of vertical forces and the drop sinks.

The paper is organized as follows. Section 2 presents a summary of the analysis of equilibrium drop shapes in the static system for the case when the line tension is neglected. The set of the minimal surface equations for each of the three interfaces is written in the form of a boundary-value problem with integral constraints that take into account the vertical force balance and satisfy the Neumann triangle condition at the triple-phase contact line. We use the method of numerical continuation implemented with AUTO (Doedel *et al.* 2007) to continue the analytically known solution that corresponds to a spherical drop for the case of zero gravity towards non-zero values of *g*. For any fixed drop volume at sufficiently small gravity *g*, there exist two different equilibrium shapes: one with a larger and one with a smaller radius of the circular triple-phase contact line. In § 3, we use the Helmholtz free energy to study the static stability of the drop and find that both equilibrium shapes can be stable for sufficiently small drops. This conclusion is experimentally verified using a small $<10\ \mu\text{L}$ water drop deposited onto the surface of a commercial vegetable oil. The effect of vertical vibration is experimentally studied in § 5.

2. Stationary floating drop

We consider a sufficiently small drop of a heavy fluid, 1, capable of floating at the interface between a lighter fluid, 2, and the ambient gas, *g*, as shown in figure 1(*a*). In equilibrium, the drop is radially symmetric. The shapes of the three interfaces that connect at the triple-phase contact line are found from the balance between the Laplace and hydrostatic pressures. A recent overview of basic phenomena related to floating droplets referred to as liquid lenses at liquid–gas interfaces, which include wetting, dewetting and hydrodynamic instabilities, can be found in the paper by Nepomnyashchy (2021). The upper part of the drop, above the horizontal dashed line, represents a sessile drop. Using a standard set of coordinates (Lohnstein 1906; Boucher, Evans & Frank 1975), the upper tip of the drop is taken as the origin of the local coordinate system, with the z_1-axis pointing downward. By introducing an angle ϕ_1 between the tangent to the drop profile at point (r_1, z_1) and the horizontal, the pressure balance yields (Lohnstein 1906; Boucher *et al.* 1975)

$$\sigma_{1g}\left(\frac{\mathrm{d}\phi_1}{\mathrm{d}s_1} + \frac{\sin(\phi_1)}{r_1}\right) = \rho_1 g z_1 + \frac{2\sigma_{1g}}{R_1}, \qquad (2.1)$$

where s_1 is the arc length of the drop profile from the origin and R_1 is the radius of curvature at the upper tip. Note that the gas density is neglected in (2.1) and (2.2).

Similarly, the lower part of the drop, below the horizontal dashed line, represents a pendant drop. The lower tip of the drop is taken as the origin of the local coordinate system, with the z_2-axis pointing upward. At point (r_2, z_2), ϕ_2 is the angle between the tangent to the drop profile and the horizontal, and s_2 is the arc length measured from the
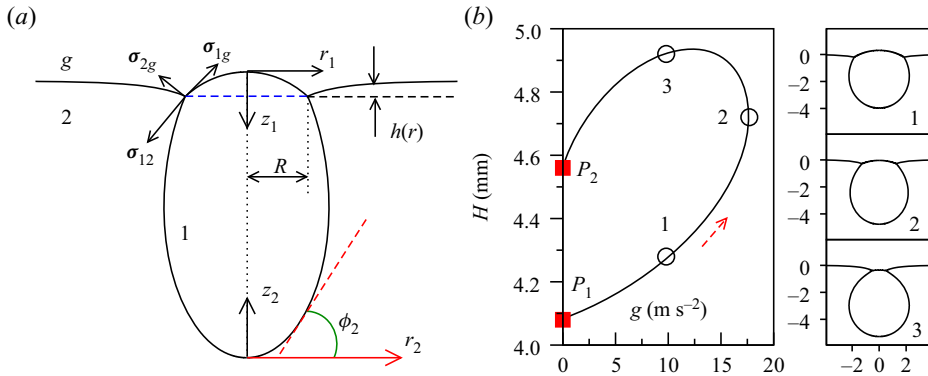
Figure 1. (*a*) A liquid drop of a heavy fluid 1 floating at the interface between a lighter fluid 2 and gas *g*. Equilibrium Neumann's triangle at the triple-phase contact line is the requirement that the net force acting on a small element of the contact line is zero, i.e. $\boldsymbol{\sigma}_{12} + \boldsymbol{\sigma}_{1g} + \boldsymbol{\sigma}_{2g} = 0$. (*b*) Variation in the total drop height H on the gravity constant g for a 50 µL water drop floating at the oil–air interface. The fluid parameters are: $\rho_1 = 1000$ kg m^{-3}, $\rho_2 = 916$ kg m^{-3}, $\sigma_{1g} = 0.045$ N m^{-1}, $\sigma_{2g} = 0.022$ N m^{-1}, $\sigma_{12} = 0.032$ N m^{-1} (Phan *et al.* 2012). The drop profiles at points 1, 2, 3 are shown on the right of the panel. Continuation starts at point P_1 that corresponds to the analytical solution given by (2.12*a*–*c*). The solution at the point P_2 corresponds to a circular drop fully submerged in fluid 2 and touching the interface $2 - g$ at a point.

lower tip. Similar to (2.1), the pressure balance can be written as (Boucher *et al.* 1975)

$$\sigma_{12}\left(\frac{d\phi_2}{ds_2} + \frac{\sin(\phi_2)}{r_2}\right) = (\rho_2 - \rho_1)gz_2 + \frac{2\sigma_{12}}{R_2}, \tag{2.2}$$

where R_2 is the radius of curvature at the lower tip. In addition to (2.1) and (2.2), the coordinates (r_i, z_i), $i = 1, 2$ satisfy

$$\frac{dr_i}{ds_i} = \cos(\phi_i), \quad \frac{dz_i}{ds_i} = \sin(\phi_i). \tag{2.3a,b}$$

Finally, the meniscus around the drop can be best described in terms of the height $h(r)$, as shown in figure 1(*a*). The requirement that pressure is constant at any given vertical level, leads to (Landau & Lifshitz 1987)

$$\sigma_{2g}\left(\frac{h''}{(1 + h'^2)^{3/2}} + \frac{h'}{r\sqrt{1 + h'^2}}\right) = \rho_2 gh - \rho_2 gh_0, \tag{2.4}$$

where a prime stands for the derivative with respect to r, h_0 denotes the height of the meniscus far away from the drop and r is the radial coordinate measured from the vertical symmetry axis of the system. The system of (2.1)–(2.4) must be solved as a boundary value problem, supplemented with the following boundary and integral constraints.

Equations (2.1) and (2.3*a,b*) with $i = 1$ are solved on the interval $0 \le s_1 \le S_1$, where S_1 is the arc length of the upper part of the drop measured from the upper tip to the triple-phase contact line. Similarly, (2.2) and (2.3*a,b*) with $i = 2$ are solved on the interval $0 \le s_2 \le S_2$, where S_2 is the arc length of the lower part of the drop measured from the lower tip to the triple-phase contact line. At the tips of the drop, we set the initial

conditions:

$$r_i(0) = z_i(0) = \phi_i(0) = 0, \quad i = 1, 2. \tag{2.5}$$

The requirement of continuity of the interface yields

$$r_1(S_1) = r_2(S_2) = R \quad \text{and} \quad z_1(S_1) = z_2(S_2), \tag{2.6a,b}$$

where R denotes the contact radius at the triple-phase contact line. Equation (2.4) is solved on the interval $R \leq r \leq \infty$ with $h(R) = 0$, $h'(\infty) = 0$ and $h(\infty) = h_0$.

The Neumann triangle, formed by three tensile forces $\boldsymbol{\sigma}_{12} + \boldsymbol{\sigma}_{1g} + \boldsymbol{\sigma}_{2g} = 0$, as shown in figure 1(*a*), reflects the requirement that the net force acting on a small element of the contact line vanishes in equilibrium. Introducing the contact angles $\Phi_i = \phi_i(S_i)$, $i = 1, 2$ between phase (*i*) and the horizontal at the triple-phase contact line, Neumann's triangle is replaced by two scalar equations:

$$\left.\begin{aligned}
0 &= \sigma_{1g} \cos(\Phi_1) + \sigma_{12} \cos(\Phi_2) - \sigma_{2g} \frac{1}{\sqrt{1 + [h'(R)]^2}}, \\
0 &= \sigma_{1g} \sin(\Phi_1) - \sigma_{12} \sin(\Phi_2) + \sigma_{2g} \frac{h'(R)}{\sqrt{1 + [h'(R)]^2}}.
\end{aligned}\right\} \tag{2.7}$$

The volumes V_i, $i = 1, 2$ of the sessile and pendant parts are given by

$$V_i = \int_0^{S_i} \pi r_i^2 \sin(\phi_i) \, \mathrm{d}s_i. \tag{2.8}$$

The total buoyancy force F_b experienced by the drop is given by the weight of fluid 2 displaced by the volume of pendant part $\rho_2 g V_2$ and the weight of fluid 2 in the cylindrical volume above the contact line level (the dashed line in figure 1*a*) with the radius R and the meniscus height h_0, i.e.

$$F_b = \rho_2 g V_2 + \rho_2 g \pi R^2 h_0. \tag{2.9}$$

Finally, the vertical force balance implies that the weight of the drop $\rho_1 g(V_1 + V_2)$ is balanced by the buoyancy force F_b and the vertical component of the surface tension force exerted by fluid 2 onto the drop. The latter is given by $2\pi \sigma_{2g} R h'(R)[1 + [h'(R)]^2]^{-1/2}$ so that the balance of vertical forces can be written in the form:

$$\rho_1 g(V_1 + V_2) = F_b + 2\pi \sigma_{2g} R \frac{h'(R)}{\sqrt{1 + [h'(R)]^2}}. \tag{2.10}$$

Recently, the minimal surface problem for a floating liquid drop has been formulated and solved to study the floatability of non-wetting drops and liquid marbles (Ooi *et al.* 2016; Wong *et al.* 2017). In particular, such a non-wetting drop corresponds to $\Phi_1 + \Phi_2 = \pi$ (or close to π) and a liquid marble is a small amount of liquid encapsulated by a thin hydrophobic powder layer. The properties of the floating state have been found to be highly sensitive with respect to variations of the surface tensions.

It should be emphasized that a direct numerical integration of the minimal surface problem ((2.1)–(2.4)) with boundary conditions ((2.5), (2.6a,b), (2.7), (2.10)) is somewhat cumbersome, as one needs to guess some of the unknowns before applying the shooting method. Here we use a much more robust and versatile numerical continuation

method AUTO (Doedel *et al.* 2007) to solve the above boundary value problem with an integral condition given by the requirement that the total volume $V_1 + V_2$ is fixed. Most importantly, the method of numerical continuation allows us to explore the entire multiplicity of all possible solutions by following a solution branch that contains saddle-node bifurcation points. Details of the numerical continuation method are summarized in Appendix A.

As a starting point of the numerical continuation method, we use the analytical solution in the case of zero gravity, when the upper and the lower parts of the drop are both spherical and the interface between fluid 2 and gas is non-deformed. By setting $h'(R) = 0$, we obtain from (2.7) the contact angles Φ_i:

$$\left.\begin{aligned}
\Phi_1 &= \cos^{-1}\left(\frac{\sigma_{1g}^2 + \sigma_{2g}^2 - \sigma_{12}^2}{2\sigma_{1g}\sigma_{2g}}\right), \\
\Phi_2 &= \cos^{-1}\left(\frac{\sigma_{12}^2 + \sigma_{2g}^2 - \sigma_{1g}^2}{2\sigma_{12}\sigma_{2g}}\right).
\end{aligned}\right\} \tag{2.11}$$

It is easy to see that the solution of (2.1)–(2.3*a*,*b*) at zero gravity is

$$\phi_i = \frac{s_i}{R_i}, \quad r_i = R_i \sin\left(\frac{s_i}{R_i}\right), \quad z_i = R_i\left[1 - \cos\left(\frac{s_i}{R_i}\right)\right], \quad 0 \le s_i \le R_i\Phi_i, \tag{2.12a–c}$$

where the radii R_i of the sessile and pendant parts are determined by the contact angles Φ_i and the horizontal radius R at the level of the contact line, i.e. $R_i \sin(\Phi_i) = R$. The volumes of the sessile and pendant parts are found from (2.8) $V_i = \pi R_i^3 (2/3 + (1/3)\cos^3(\Phi_i) - \cos(\Phi_i))$.

Our aim is to show the possibility of multiple equilibrium shapes of a floating drop with a given volume. We therefore present our numerical results for a particular choice of fluid parameters reported by Phan *et al.* (2012). A systematic study can be conducted similar to that of Wong *et al.* (2017), by using standard non-dimensional parameters such as the Bond number $Bo = R^2\rho_1 g/\sigma_{1g}$, the ratios of the fluid densities ρ_1/ρ_2, and surface tensions σ_{1g}/σ_{12} and σ_{1g}/σ_{2g}.

First, we continue the solution (2.12*a–c*) using g as a principle continuation parameter. The total height of the drop $H = z_1(S_1) + z_2(S_2)$ is displayed as a function of g in figure 1(*b*). The continuation starts at the point P_1 that corresponds to the analytical solution (2.12*a–c*). As g increases, the drop profile changes, as shown by the three selected solutions 1, 2, 3 on the right of figure 1(*b*). No stationary solutions exist past the saddle-node bifurcation point (solution 2) in terms of g. For any g below the saddle-node point, there exist two stationary drop profiles: one with a lower value of the radius R (solution 1) and one with a larger value of R (solution 3). At vanishingly small g, the second solution (point P_2) collapses to a spherical drop fully submerged in fluid 2 that only touches the interface $2 - g$ at one point.

After the value of $g = 9.8$ m s^{-2} is reached, the solution is followed using AUTO (Doedel *et al.* 2007) with the drop volume V as a continuation parameter. The radius R of the contact line is shown as a function of V in figure 2(*b*). Two different drops with the identical volume $V = 90$ μL are shown in figure 2(*a*).

It is remarkable that multiple stationary profiles of floating drops have never been studied in detail. In an early study (Hartland & Burri 1976), the existence of multiple profiles has been mentioned, but the solutions with the smaller value of R were declared unstable. The reason for the instability (Hartland & Burri 1976) was the qualitative
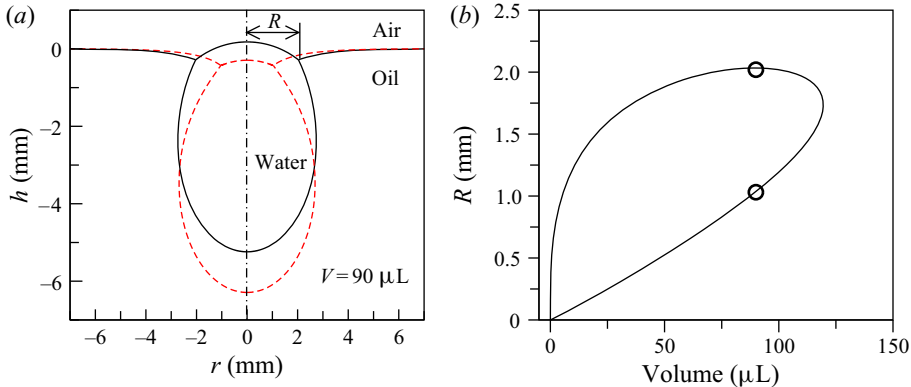
Figure 2. (*a*) Two water drops with the identical volume $V = 90$ µL at the oil–air interface. (*b*) Contact line radius R as a function of the volume V at $g = 9.8$ m s^{-2}. Circles indicate the location of the solutions in (*a*).

comparison of a floating drop with a heavy rigid sphere capable of floating on the surface of a fluid that does not wet the surface of the sphere (Hartland & Robinson 1971). Indeed, in the case of a rigid sphere, the stability condition is derived by looking at the position of the centre of mass $z_c(g)$ of the sphere as a function of the gravity constant g. Thus, if g is slightly increased (decreased), the centre of mass of a stable configuration must descend (ascend) so that after g is set back to its original value, the sphere will bounce back up (down) to recover the original stationary position. It was shown (Hartland & Robinson 1971) that solutions with a larger radius of the contact line are stable, while those with the smaller value of radius are unstable. However, to the best of our knowledge, no such calculations are available for a floating liquid drop. A comprehensive stability analysis that takes into account static and dynamic perturbations is still missing.

3. Static stability of a floating drop

We approach the stability of a floating drop from the point of view of the Helmholtz free energy, by considering the so-called static axisymmetric perturbations of the drop profile that satisfy the Laplace pressure balance. Such static stability analysis neglects the motion of the fluids and, therefore, can only be considered as a precursor to the true dynamic stability with respect to non-axisymmetric perturbations. Note that a similar method has been applied to study the static stability of pendant drops hanging from a solid plate (Padday & Pitt 1973).

We take the level of the carrier fluid 2 far away from the drop as a zero level for the vertical axis directed upwards, as shown in figure 3. The excess total energy E_t of the system is constructed not counting the infinite energy of the semi-infinite fluid 2 with a flat fluid–gas interface in the absence of the drop. The excess surface energy is

$$E_s = \sigma_{12}S_{12} + \sigma_{1g}S_{1g} + \sigma_{2g}S_{2g}, \tag{3.1}$$

where $S_{12} = \int_0^{S_2} 2\pi r_2 \, ds_2$ and $S_{1g} = \int_0^{S_1} 2\pi r_1 \, ds_1$ are the surface areas of the fluid 1–fluid 2 and fluid 1–gas interfaces and $S_{2g} = \int_R^{\infty} 2\pi r(\sqrt{1 + h'^2} - 1) \, dr - \pi R^2$ is the excess surface area of the fluid 2–gas interface. The excess potential energy of the
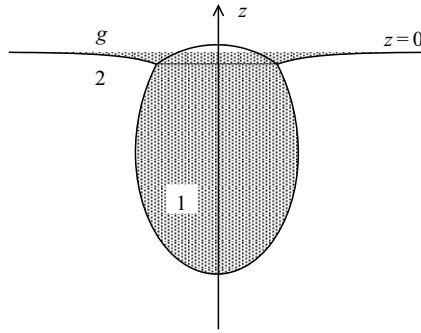
922 A31-7

Figure 3. Excess potential energy U_e of the fluid bath is given by the potential energy of the shaded part filled with fluid 2 with negative density $-\rho_2$.

system is

$$E_p = Mgz_c + U_e, \tag{3.2}$$

where $M = \rho_1(V_1 + V_2)$ is the total mass of the drop, z_c is the vertical coordinate of the centre of mass of the drop and U_e is the excess potential energy of the fluid bath. Then, U_e can be further represented in the form:

$$U_e = -g\rho_2 V_e Z_e, \tag{3.3}$$

where V_e is the volume of the shaded part in figure 3 and Z_e is the coordinate of the centre of mass of the shaded part in figure 3, filled with a homogeneous density. The excess total energy E_t is thus given by $E_t = E_p + E_s$. Note that the values z_c, Z_e, V_e and E_s depend on g, thus

$$z_c = z_c(g), \quad Z_e = Z_e(g), \quad V_e = V_e(g), \quad E_s = E_s(g). \tag{3.4a–d}$$

Now let us assume that the gravity constant has been slightly changed to $g + \delta g$. This can be practically achieved by placing the system in a lift that accelerates either upward or downward, or alternatively, as a result of a displacing disturbance of the system that is localized in time. The drop will assume a new stationary shape that corresponds to the new value of $g + \delta g$. Now assume that the lift (or the disturbance) suddenly stops and the gravity constant is instantaneously set back to the original value g. At this moment of time, the drop and meniscus still have new shapes, so that the total energy of the system is

$$\tilde{E}_t = Mgz_c(g + \delta g) - g\rho_2 V_e(g + \delta g)Z_e(g + \delta g) + E_s(g + \delta g). \tag{3.5}$$

The system is stable if $\tilde{E}_t > E_t$, i.e.

$$\begin{aligned} \tilde{E}_t - E_t = {} & Mgz_c(g + \delta g) - Mgz_c(g) \\ & - g\rho_2 V_e(g + \delta g)Z_e(g + \delta g) + g\rho_2 V_e(g)Z_e(g) \\ & + E_s(g + \delta g) - E_s(g) > 0. \end{aligned} \tag{3.6}$$

Expanding (3.6) into powers of δg, we obtain the leading term:

$$\delta E_t = \left(Mg\frac{\mathrm{d}z_c(g)}{\mathrm{d}g} - g\rho_2\frac{\mathrm{d}(V_e Z_e)}{\mathrm{d}g} + \frac{\mathrm{d}E_s(g)}{\mathrm{d}g} \right)\delta g = 0, \tag{3.7}$$

which must vanish for arbitrary small δg, because the drop shape at the original value of g is in equilibrium.

922 A31-8

Differentiating $\delta E_t/\delta g = 0$ with respect to g, we obtain:

$$\frac{\mathrm{d}}{\mathrm{d}g}\left(\frac{\delta E_t}{\delta g}\right) = M\frac{\mathrm{d}z_c(g)}{\mathrm{d}g} + Mg\frac{\mathrm{d}^2 z_c(g)}{\mathrm{d}g^2} - \rho_2\frac{\mathrm{d}(V_e Z_e)}{\mathrm{d}g} - g\rho_2\frac{\mathrm{d}^2(V_g Z_g)}{\mathrm{d}g^2} + \frac{\mathrm{d}^2 E_s(g)}{\mathrm{d}g^2} = 0. \tag{3.8}$$

The second term in the expansion of (3.6) in terms of δg is

$$\delta^2 E_t = \left(Mg\frac{\mathrm{d}^2 z_c(g)}{\mathrm{d}g^2} - g\rho_2\frac{\mathrm{d}^2(V_e Z_e)}{\mathrm{d}g^2} + \frac{\mathrm{d}^2 E_s(g)}{\mathrm{d}g^2}\right)\delta g^2 > 0. \tag{3.9}$$

Equation (3.8) can now be used to remove the second derivative terms in (3.9) and to finally obtain the static stability condition:

$$\rho_2\frac{\mathrm{d}(V_e Z_e)}{\mathrm{d}g} - M\frac{\mathrm{d}z_c(g)}{\mathrm{d}g} > 0. \tag{3.10}$$

Equation (3.10) is now recast in the form $\mathrm{d}f(g)/\mathrm{d}g < 0$, where

$$f(g) = z_c(g) - \frac{\rho_2 V_e(g)Z_e(g)}{\rho_1 V}, \tag{3.11}$$

and V is the fixed drop volume. Function $f(g)$ can be expressed in terms of the variables z_i, ϕ_i, r_i and $h(r)$ from (2.1)–(2.3a,b), as shown in Appendix B.

Function $f(g)$ in (3.11) coincides with the excess potential energy (3.2) per weight of the drop Mg, i.e. $f(g) = E_p(g)/(Mg)$.

The function $f(g)$ from (3.11) is shown in figure 4(a) for three different volumes $V = 50, 20$ and $10\,\mu\text{L}$ of a water drop on oil surface with fluid parameters as in figure 1(b). Statically stable shapes correspond to $\mathrm{d}f/\mathrm{d}g < 0$, as indicated by the thick solid curves, whereas statically unstable states are marked by the thick dashed parts of the curves. For each volume, the zero-gravity solution given by (2.12a–c) has a larger value of $f(g = 0)$. At any fixed value of g below the saddle-node bifurcation point, the solution with larger (smaller) values of the contact radius R belongs to the upper (lower) branch of $f(g)$. At terrestrial gravity of $g = 9.8\,\text{m s}^{-2}$, as indicated by the vertical line in figure 4, larger drops with a volume $V > 20\,\mu\text{L}$ have only one stable shape with a larger value of R (upper branch). However, smaller drops with a volume $V < 20\,\mu\text{L}$ have two stable shapes: one with a larger (upper branch) and one with a smaller (lower branch) contact radius R.

A simple physical interpretation of the static stability analysis conducted here can be obtained if we note that the function $f(g)$ can be approximated by the scaled vertical coordinate of the centre of mass of the drop $(1 - \rho_1/\rho_2)z_c$. Indeed, this result immediately follows from (3.11) if V_e is replaced by the drop volume V, i.e. $f(g) \approx z_c(g) - (\rho_2 V Z_e(g))/\rho_1 V = (1 - \rho_1/\rho_2)z_c$. The function $(1 - \rho_1/\rho_2)z_c$ is represented by thin solid lines in figure 4(a) alongside each of the three $f(g)$ curves.

Now the interpretation of the static stability is similar to that by Hartland & Robinson (1971), where the dynamic equilibrium of a rigid sphere at the deformable liquid–liquid interface was studied. Namely, the drop is stable if its centre of mass is lowered (raised) when g is increased (decreased), i.e. $\mathrm{d}z_c(g)/\mathrm{d}g < 0$. On the other hand, the drop is unstable if $\mathrm{d}z_c(g)/\mathrm{d}g > 0$. Indeed, assume that $\mathrm{d}z_c(g)/\mathrm{d}g < 0$ and the drop is in equilibrium at $g = g_0$. In equilibrium, the net upward force F_u is equal to the weight of the drop, i.e $F_u(g_0) = Mg_0$. When the value of g is slowly increased by a small margin $g_0 \rightarrow g_0 + \delta g$, the weight of the drop increases to $(g_0 + \delta g)M$. If the increase of g occurs slowly, the drop remains in equilibrium during this process so that this new weight is again balanced by the
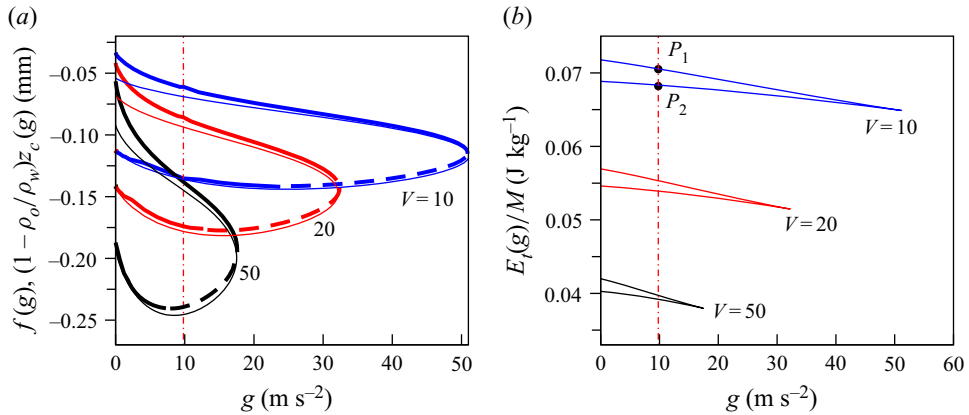
Figure 4. (*a*) Function $f(g)$ given by (3.11) determined for $V = 50$, 20 and 10 μL water drop floatation on oil with the parameters as in figure 1(*b*). Stable (unstable) solutions are marked by the thick solid (thick dashed) lines. The zero gravity solution given by (2.12*a–c*) corresponds to the larger value of f at $g = 0$. For each volume, the solutions on the upper branch have a larger contact radius R. Drops smaller than 20 μL have two stable floatation shapes at $g = 9.8$ m s^{-2}: one with a larger and one with a smaller value of the contact radius. Thin solid lines represent the scaled vertical coordinate of the centre of mass of the drop $(1 - \rho_1/\rho_2)z_c$. (*b*) Total excess energy of the drop $E_t = E_p + E_s$ per drop mass $M = \rho_1 V$ for $V = 50$, 20 and 10 μL water drops. At terrestrial gravity $g = 9.8$ m s^{-2}, the point on the lower (upper) branch corresponds to equilibrium shape with a larger (smaller) contact radius.

upward force $F_u(g_0 + \delta g) = (g_0 + \delta g)M$. Because we assumed that $\mathrm{d}z_c(g)/\mathrm{d}g < 0$, the centre of mass of the drop is lowered. When g is quickly set back to its original value g_0, the weight of the drop is instantaneously changed back to Mg_0, but the position of the centre of mass of the drop and the net upward force are still $z_c(g_0 + \delta g)$ and $F_u = (g_0 + \delta g)M$, respectively. It is now clear that vertical forces are no longer in balance and the drop will bounce back upwards to regain its original position. This corresponds to the stable configuration.

4. Contact radius of a μL-sized water drop floating on commercial oil

We conduct a series of experiments with millimetre-sized (μL in volume) water drops on the surface of commercial oil to demonstrate the existence of multiple equilibrium values of the contact radius of the triple-phase contact line. We use two different methods to deposit a small quantity of water <10 μL onto the surface of a commercial vegetable oil. To obtain a shape with a smaller contact radius, we use a similar technique as that used by Phan *et al.* (2012), namely, a pendant water drop with the maximal possible volume is produced freely hanging in air from a pipette with the diameter of the nostril of 2.5 mm. After the drop is carefully brought into contact with the oil surface, it separates from the pipette and starts to float on the oil surface, as shown in figure 5(*a*). In the second deposition method, we produce a drop with a similar volume hanging freely from a pipette. The drop is carefully brought into contact with a vertical wall of the polystyrene container filled with oil. The drop slowly slides down the wall under the action of gravity and eventually comes into contact with the meniscus formed by oil. The spreading coefficient of water on oil is generally larger than that of water on polystyrene. Therefore, the drop is pulled by capillary forces away from the container wall. This process creates the second stable shape with a
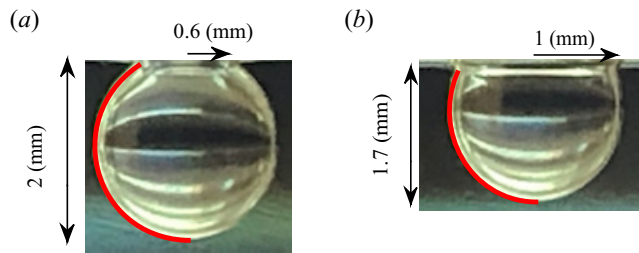
Figure 5. Two stable shapes of a water drop with approximately identical volume 5 ± 0.5 µL floating on the surface of a commercial vegetable oil. The thick solid line is obtained by fitting the experimental drop profile with a pendant drop solution of (2.2), (2.3*a,b*) with the fluid parameters as in figure 1 and the fitted value of the radius of curvature at the lower tip $R_2 \approx 1.13$ mm in both cases. The shape with a smaller contact radius (*a*) is obtained by depositing a drop from a pipette directly onto the oil surface. The shape with the larger contact radius (*b*) is obtained by depositing the drop from the pipette onto the vertical wall of the container and allowing the drop to slowly slide down the wall to touch the oil surface.

larger contact radius, as shown in figure 5(*b*). In both cases, the estimated volume of the water drops is approximately identical $V \approx 5 \pm 0.5$ µL. The video demonstrating both deposition methods is available in the supplementary material available at https://doi.org/10.1017/jfm.2021.546.

The drops are photographed and the contours of their pendant parts submerged in oil are extracted using Matlab. Note that the contour of the upper cap of the drop is difficult to extract, as it is obstructed by the meniscus formed by oil with the container wall. The experimentally obtained profiles are fitted by the analytical solution of the pendant drop (2.2) and (2.3*a,b*) with fluid parameters as in figure 1. We use the radius of curvature at the lower tip R_2 as the fitting parameter and obtain the value of $R_2 \approx 1.13$ mm for both shapes. The analytical solution is shown by the thick solid line in figure 5. The volumes of the submerged parts, determined using the fitted analytical solution, are found to be 6 µL in figure 5(*a*) and 5 µL in figure 5(*b*). The difference in volumes arises from the unaccounted volume of the obstructed upper caps.

In the next experiment, we observe a mechanically induced transition from the configuration in figure 5(*a*) to the configuration in figure 5(*b*). A clean metallic needle is gently dipped into the upper part of the drop through the water–air interface. A small amount of water displaced by the needle rises to push the contact line outwards. After the needle is removed the drop remains in the configuration with a larger contact radius. The video demonstrating the experiment is available in the supplementary material.

Before comparing the above experiments with our findings in § 3, a word of caution is in order. It is notoriously difficult to control the surface tension in experiments with very small quantities of fluids (µL drops), which are in contact with other seemingly immiscible fluids. In particular, the water–air surface tension in the presence of oil is lowered to ≈ 0.045 (N m^{-1}) (Phan *et al.* 2012) as compared with the surface tension of an infinitely large water–air interface with the standard value of ≈ 0.072 (N m^{-1}) at room temperature. This arises from cloaking of the upper part of the drop by a thin oil film (Smith *et al.* 2013). It is therefore plausible that the thickness of this oil film and, as a result, the effective surface tension of the upper part of the drop may also depend on the radius of the contact line. In addition, the line tension is neglected in the theoretical model used here, while some experimental studies report equilibrium floating drops that do not satisfy the Neumann triangle (George *et al.* 2016). All these factors may contribute to the multiplicity of the contact radius observed here.

Assuming that multiple equilibrium configurations of a floating drop are linked to the bistability found in § 3, we describe the transition from a smaller to a larger contact radius in terms of the total excess energy $E_t = E_p + E_s$ per mass of the drop M. In figure 4(*b*) we plot $(E_p + E_s)/M$ versus g for three water drops with volumes $V = 10, 20, 50$ μL. The configuration with a smaller contact radius corresponds to a higher value of excess energy (point P_1 on the curve for $V = 10$ μL). After the contact line expands, the excess energy of the drop is decreased (point P_2 on the curve for $V = 10$ μL).

5. Vertical vibration helps liquid drops to stay afloat

To investigate how external vertical vibration affects the floatability of the drop, we conduct a series of experiments with drops of distilled water with the volume $V \lesssim 0.15$ mL deposited on top of a vertically vibrated 1 cm thick layer of commercial olive oil. The oil was placed in a circular container with the diameter of 10 cm mounted on a 6.5" 45 W RMS audio speaker (Sony, Japan) powered by a 30 W stereo amplifier (Yamaha TSS-15, China) of a sinusoidal signal produced by a digital tone generator. The container was vertically vibrated at frequencies in the range 40–80 Hz. The vibration amplitudes were sufficiently large to excite subharmonic Faraday waves on the surface of the water drop but not strong enough to excite Faraday waves on the free surface of the oil layer.

The vertical coordinate of the container $z_p(t)$ oscillates with the amplitude A and the period $T = 1/f$ according to

$$z_p(t) = A \cos(\phi + 2\pi t/T), \tag{5.1}$$

where f is the frequency in Hertz and ϕ is a fixed phase. In the co-moving frame of reference, the time-dependent downward acceleration is

$$g + \ddot{z}_p(t) = g - A \left(\frac{2\pi}{T}\right)^2 \cos(\phi + 2\pi t/T), \tag{5.2}$$

where $\dot{z}$ stands for the time derivative of z.

We use the ADXL 326 accelerometer (Analog Devices, USA) attached to the container and a digital oscilloscope (Tektronix TDS 210, USA) to measure the acceleration amplitude $a/g = A(2\pi f)^2/g$ in units of g. The motion of the drop was recorded at up to 240 f.p.s. using a high-speed camera and the obtained images were post-processed in Matlab for further analysis.

As a first step, we determine the maximal possible volume of a water drop V_m that hangs at the olive oil–air interface without vibration and find that $V_m \approx 0.1$ mL. Note that with a commercial vegetable oil, a stable hanging water drop of up to 0.17 mL can be achieved (Phan *et al.* 2012). Such a drop stretches down to reach a vertical size of 1 cm and more owing to a larger value of the vegetable oil–air surface tension. To avoid any direct contact between the drop and the bottom of the 1 cm deep container used in our experiments, we have chosen olive oil over vegetable oil. The surface tension between olive oil and water is 25 ± 13 mN m^{-1} and between olive oil and air is 46 ± 6 mN m^{-1}, as estimated by Pototsky *et al.* (2020). The typical value of the dynamic viscosity of the olive oil is 30 mPa s (Sahasrabudhe *et al.* 2017).

Previous studies have demonstrated that liquid lenses of a lighter fluid floating on the surface of a heavier and more viscous fluid undergo a spontaneous horizontal elongation under the action of vertical vibration (Pucci *et al.* 2011, 2013; Pucci, Ben Amar & Couder
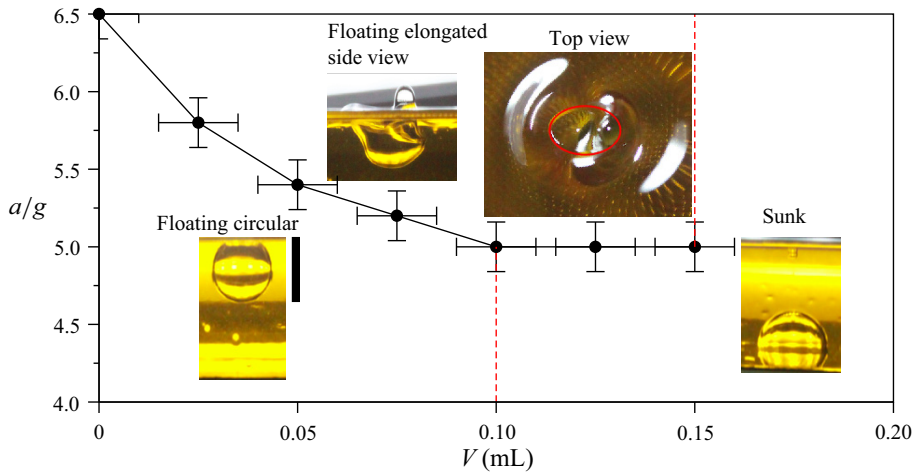
Figure 6. Phase diagram separating floating circular, floating elongated and sinking water drops vibrated at 60 Hz in olive oil. Symbols indicate an experimentally determined critical acceleration a/g, that corresponds to the onset of the Faraday instability in a hanging water drop of a varying volume. In the absence of vibration, smaller drops with $V \lesssim 0.1$ mL hang at the oil–air interface, while larger drops $V \gtrsim 0.1$ mL sink to the bottom of the container. For 0.1 mL $\lesssim V \lesssim 0.15$ mL the drop floats at the oil–air interface when vibrated with the amplitude $a/g > 5$. Insets: representative snapshots of a floating circular, floating elongated and a sunk water drop. The vertical scale bar next to the floating circular drop indicates a length of 5 mm. An ellipse (solid line) in the top view of the floating elongated drop highlights an approximate location of the contact line. The ratio between the major and the minor axes of the ellipse is 2 : 3.

2015; Pototsky & Bestehorn 2018). The underlying physical mechanism was traced down to the Faraday instability at the upper drop surface. The onset of the Faraday instability corresponds to a period-doubling bifurcation (Pototsky & Bestehorn 2018): the lens starts to oscillate at half of the driving frequency and elongates horizontally in a randomly chosen direction. The resultant equilibrium shape of the elongated lens, as seen from the top, is dictated by the balance between the radiation pressure of the unidirectional Faraday waves and the Laplace pressure which always tries to return the lens back into a circular shape (Pucci *et al.* 2011, 2013).

Here we observe that similar to floating lenses, a heavy water drop that floats on the surface of a lighter and more viscous oil also undergoes a horizontal elongation when Faraday waves are excited on the upper drop surface. Remarkably, the floatability of the elongated drop increases, which allows drops with volumes greater than the maximal static volume $V_m \approx 0.1$ mL to stay afloat.

Our experimental protocol consists of a careful deposition of a water drop of various volumes with a pipette on the surface of the vibrated oil bath, and different acceleration amplitudes a. Below the Faraday instability threshold, the drop assumes a circular shape when viewed from the top, as seen in the upper right inset of figure 6 (top view). A side view of such a floating circular drop is also shown in the inset of figure 6 (floating circular). Above the Faraday threshold the drop elongates, as displayed in the inset in figure 6 (floating elongated). The shape of the contact line in the elongated state is approximately elliptic with a relatively small eccentricity (ratio of the major and minor axes) of 2 : 3. In contrast to an anticipated destructive effect of shaking, the drop continues to float when vibrated at up to $a = 6.5g$. For $a > 6.5g$, the Faraday instability in the oil layer sets in.

922 A31-13

Following this protocol we record the Faraday stability threshold for different drop volumes in figure 6 vibrated at $f = 60$ Hz (a representative value). The vertical and horizontal error bars indicate the uncertainty in measurements of the acceleration amplitude and the drop volume, respectively.

Our goal is to demonstrate the fundamental possibility to increase drop floatability by vibration. A detailed experimental investigation, where a wide range of frequencies and fluid parameters is tested, falls beyond the scope of this study. We choose to present the main results of this section for the driving frequency of $f = 60$ Hz owing to the technical limitations of our experimental set-up. Thus, the critical vibration amplitude of the Petri dish required to excite the Faraday waves in the drop increases with the driving frequency. The power of the amplifier used in our experiments only allows us to reach the Faraday threshold in mL-volume water drops up to the frequencies of $f \approx 70$–80 Hz. On the other hand, at lower frequencies $f < 50$ Hz the onset amplitudes for Faraday waves in a water drop and in the oil film are very close, so that oil surface develops large amplitude waves close to the triple-phase contact line. These large deformations of the oil surface have a detrimental effect on the drop floatability.

To confirm that the effect of increased floatability can be found for a range of driving frequencies, we demonstrate the floatation of a 0.12 mL water drop vibrated at $f = 50$ Hz. When the vibration is switched off, the drop can no longer stay afloat and sinks. The video of the experiment is available in the supplementary material.

We found that drops with the volume 0.1 mL $< V <$ 0.15 mL can float at the oil–air interface when vibrated at $a > 5g$. These drops will otherwise sink to the bottom of the container when the vibration amplitude is reduced below $a < 5g$. Notably, the action of vibration delays the emergence of the critical event of drop sinkage similar to delaying of film rupture (Sterman-Cohen *et al.* 2017) or delaying of liquid bridge breaking (Benilov 2016).

5.1. *The origin of the excess lifting force*

To understand the physical mechanism responsible for the excess lifting force required to keep larger drops afloat, we consider the balance of the vertical forces acting on the drop averaged over at least two forcing periods $2T$:

$$Mg = \langle F_b \rangle + \langle F_t \rangle, \tag{5.3}$$

where M is the total mass of the drop, F_b is the buoyancy force, F_t is the lifting force owing to surface tension acting at the triple-phase oil–water–air contact line and $\langle \cdots \rangle = (2T)^{-1} \int_0^{2T} (\ldots) \, dt$ denotes averaging over time. Note that averaging over $2T$ is necessary owing to a subharmonic nature of the Faraday waves.

Similar to (2.10) in the static case, the instantaneous value of F_t for the elongated drop can be represented in the form:

$$F_t = \sigma_{2g} \int_{C(t)} \sin(\alpha(l, t)) \, dl, \tag{5.4}$$

where $\alpha(l, t)$ is the local instantaneous contact angle between the oil–gas interface and the horizontal, and the integration contour $C(t)$ represents the instantaneous shape of the contact line of the elongated drop, parametrized by the arc length l. In the static case, $\sin(\alpha(l, t)) = h'(R)/\sqrt{1 + [h'(R)]^2}$ is constant and C is a circle with the radius R so that (2.10) is recovered.

922 A31-14

The excess lifting force can be explained if $\langle F_t \rangle$ is larger than its static value, given by $2\pi R\sigma_{2g}h'(R)/\sqrt{1 + [h'(R)]^2}$. However, it is important to emphasize that the average value of the integral in (5.4) cannot be simply estimated, owing to the time-dependent contact angle $\alpha(t, l)$, as can be appreciated from the side view of the floating elongated drop in the inset in figure 6.

As we explain below, the estimation of the average value of the buoyancy force $\langle F_b \rangle$ is experimentally easier to access than the estimation of $\langle F_t \rangle$. We therefore proceed to show that $\langle F_b \rangle$ measured for the vibrated drop is, in fact, smaller than the static value of a fully submerged drop, i.e. $\langle F_b \rangle < (\rho_1 - \rho_2)gV_0$, where V_0 represents the total volume of the drop. This confirms that the excess lifting force arises from the increased value of $\langle F_t \rangle$.

We record a side-view slow motion video of a 0.12 mL drop. To increase the contrast with the yellow oil, we add a small amount of red food colouring to the water. The drop is stretched horizontally and the stretching direction is perpendicular to the view line of the camera, as shown in the inset in figure 6.

Individual frames are extracted from the slow motion video and post-processed in Matlab to detect the contour of the drop. Figure 7(*a*) displays 50 contours of the upper part of the drop exposed above the oil–air interface. The time interval between any two neighbouring contours is 1/200 s. For comparison, we show in figure 7(*b*) the vertical coordinate of the vibrating container $z_c(t)$ in the laboratory frame. It is clear that the drop oscillates sub-harmonically at half of the driving frequency $f/2 = 30$ Hz. The left and the right edges of the drop periodically bulge out to develop a small blob every 1/30 s in anti-phase to each other. The slow motion video of the floating drop in figure 7 is available in the Supplement.

Before proceeding, we estimate the average dynamic pressure P_d acting on the water–oil interface at the submerged part of the drop. Owing to continuity of the velocity field, the difference of the dynamic pressures in oil and water is given by $P_d = |\rho_1 - \rho_2|u^2$, where ρ_1 and ρ_2 are the densities of water and oil, respectively. The typical velocity inside the water drop can be extracted from figure 7(*a*). The maximal height of the blobs periodically developing above the oil–air interface are $\sim 1, \ldots, 3$ mm. Because the blobs develop over the interval of time $1/f = 1/60$ s, the average speed associated with this motion is $u \sim 10^{-1}$ m s^{-1}. This yields the average dynamic pressure at the oil–water interface of $P_d \sim |\rho_1 - \rho_2| \times 10^{-2}$ N m^{-2}. The dynamic pressure must be compared with the hydrostatic pressure $P_s = |\rho_1 - \rho_2|gh$, where $h \approx 10^{-2}$ m is the vertical size of the drop. Thus, we estimate that the dynamic pressure $P_d \approx 10^{-1}P_s$ can be neglected. The total buoyancy force is given by

$$\langle F_b \rangle = (\rho_1 - \rho_2)\langle(g + \ddot{z}_p(t))V_s(t)\rangle, \tag{5.5}$$

where $V_s(t)$ is the time-dependent volume of the oil displaced by the drop.

We assume $V_s(t) \approx V_0 - \Delta V(t)$, where V_0 is the total volume of the drop and $\Delta V(t) \geq 0$ is the instantaneous volume of the part of the drop above the oil–air interface. It is important to note that this assumption neglects the existence of the air pockets (dark regions in the insets in figure 6). Finally, we obtain

$$\langle F_b \rangle = (\rho_1 - \rho_2)(gV_0 - \langle\ddot{z}_p(t)\Delta V(t)\rangle - g\langle\Delta V(t)\rangle), \tag{5.6}$$

where $\langle\ddot{z}_p(t)\rangle = 0$ was used. Equation (5.6) shows that the average buoyancy force $\langle F_b \rangle$ is larger than the static buoyancy $(\rho_1 - \rho_2)gV_0$ only if $\langle\ddot{z}_p(t)\Delta V(t)\rangle + g\langle\Delta V(t)\rangle < 0$.
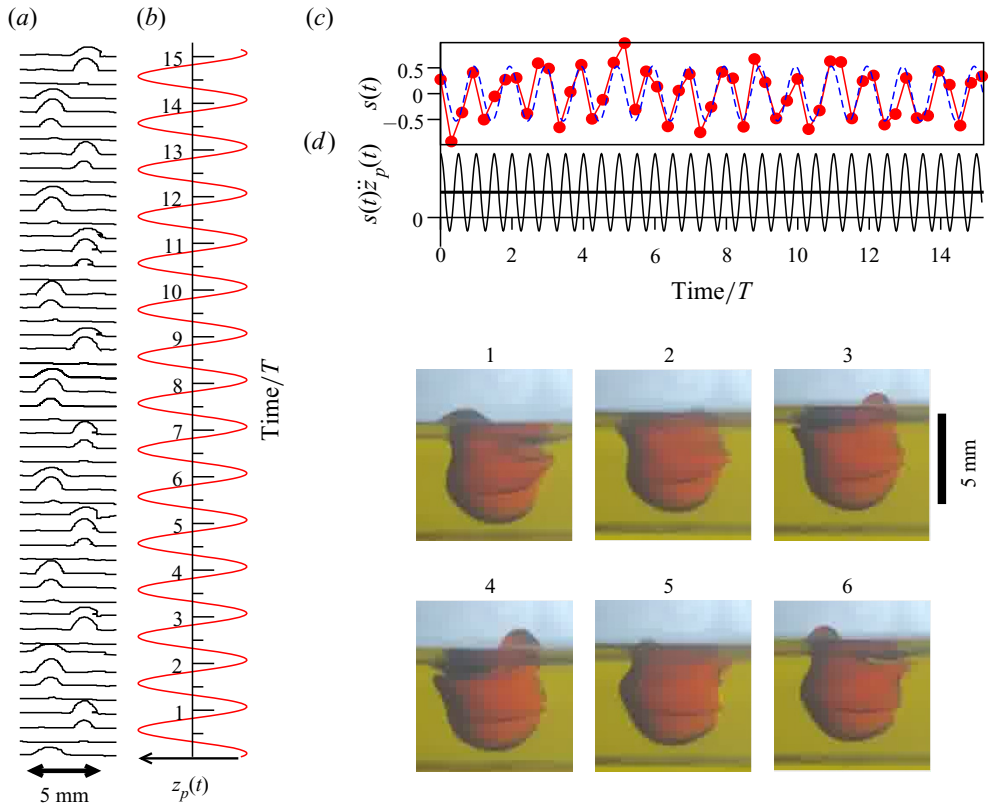
Figure 7. (*a*) Series of 50 contours of the upper part of a 0.12 mL floating drop vibrated at 60 Hz extracted from a 200 f.p.s. slow motion video. The vertical axes in (*a,b*) represent time in the units of the vibration period $T = 1/60$ s. The horizontal axis in (*b*) is the vertical coordinate of the container $z_p(t)$ vibrating at 60 Hz. (*c*) Circles correspond to the scaled volume factor $s(t)$ associated with the upper part of the drop above the oil–air interface estimated from (*a*). The dashed curve in (*c*) is the fitting line $\sim S_0 \cos(\psi + 2\pi t/T)$ to the experimental data. (*d*) The function $s(t)\ddot{z}_p(t)$ together with its time-average value represented by the thick horizontal line. Photographs 1–6 display snapshots of the drop showing also the blobs emerging above the oil–gas interface. The six snapshots correspond to the first six contours in (*a*) from the time interval between 0 and $1.5T$.

Note that the average of a product of two sinusoidal functions $\langle f(t)g(t + \phi)\rangle$ with a zero average value $\langle f(t)\rangle = \langle g(t)\rangle = 0$ can be positive or negative depending on the phase shift between them. For example, $\langle a\cos(\omega t)\cos(\phi + \omega t)\rangle = a\cos(\phi)/2$.

Our analysis is continued to show that $\langle \ddot{z}_p(t)\Delta V(t)\rangle > 0$, which together with $\langle \Delta V(t)\rangle > 0$ implies that the average buoyancy force is smaller than the static buoyancy $\langle F_b\rangle < (\rho_1 - \rho_2)gV_0$. To show that $\langle \ddot{z}_p(t)\Delta V(t)\rangle > 0$, we assume that the true volume $\Delta V(t)$ of the upper part of the drop is proportional to the area $S(t)$ under the two-dimensional drop contour shown in figure 7(*a*). The scaled normalized area $s(t) = S(t)/\langle S(t)\rangle - 1$ is calculated for each of the 50 profiles in figure 7(*a*) and presented versus time in figure 7(*c*). The data are fitted by $S_0 \cos(\psi + 2\pi t/T)$ shown by the dashed line in figure 7(*c*). The function $\ddot{z}_p(t)s(t)$ is also shown in figure 7(*c*) along with the time-average value represented by the thick horizontal line. Because $\langle \ddot{z}_p(t)s(t)\rangle > 0$, we finally conclude that $\langle \ddot{z}_p(t)\Delta V(t)\rangle > 0$.

922 A31-16

Consequently, the floatation of the drop is necessarily enabled by the increased surface tension force $\langle F_t \rangle$, which supports the drop at the triple-phase contact line. The average $\langle F_t \rangle$ becomes larger than the corresponding force in the static case, owing to the increased total length of the contact line in a horizontally elongated drop, as observed in our experiments.

In support of the above findings and to better visualize the lifting effect of the vibration, we deposit 0.15 mL of water on the surface of a 5 mm thick layer of olive oil. In the absence of vibration, the water drop sinks to the bottom of the Petri dish, thus making a puddle. When the puddle is vibrated at 60 Hz with an amplitude of $a > 4g$, it stretches horizontally driven by Faraday waves. Eventually, the entire volume of water is drawn to the oil–air interface and the water drop floats without touching the bottom of the Petri dish. We record a side-view slow motion video of the moment of take-off of the water puddle, and this is available in the supplementary material.

6. Conclusion

To conclude, we have studied theoretically and experimentally the stability and dynamics of a liquid drop of a heavier fluid floating on the surface of a lighter and more viscous fluid. In equilibrium, small drops may stay afloat assuming two different radially symmetric shapes, one is characterized by a smaller and one by a larger radius of the triple-phase contact line. Static stability analysis reveals that both shapes can be stable at terrestrial gravity if the volume of the drop is below a certain critical value.

As the volume of the drop is gradually increased beyond this certain critical volume, the shape with a smaller contact radius loses its stability and the drop sinks. The second stable shape with a larger contact radius remains stable until another critical volume is reached, beyond which no static floating drops exist.

Experiments conducted with µL-sized water drops on commercial oil confirm the existence of multiple equilibrium radii of the triple-phase contact line. However, the exact physical origin of the observed multistability is yet to be identified. Thus it is plausible that either the line tension or the variable surface tension of the upper cap of the drop might lead to multiple stable menisci configurations.

Remarkably, the floatability of the drop can be slightly increased if the drop is vibrated vertically with the frequency of Hz-order. We have performed a series of experiments with water drops on an olive oil surface and found that drops with the volume between 0.1 mL and 0.15 mL remain afloat when vibrated at 60 Hz with the acceleration amplitude between $5g$ and $6g$. In the absence of vibration, water drops larger than 0.1 mL detach from the oil surface and sink. The origin of the excess lifting force is rooted in the horizontal elongation of the drop, driven by the unidirectional Faraday waves that develop on the upper drop surface. The average length of the contact line in an elongated state appears to be larger than in a static radially symmetric shape. As a result, the average lifting force exerted by tensile forces increases, which allows for heavier drops to stay afloat when vibrated.

Finally, the results presented here, apart from their academic interest, may serve as a basis for research in emulsification of dispersed systems containing several immiscible liquids of different densities and be used in pharmaceutical applications for the stabilization of emulsions in their suspended state by shaking.

Supplementary movies. Supplementary movies are available at https://doi.org/10.1017/jfm.2021.546.

Declaration of interests. The authors report no conflict of interest.

Author ORCIDs.
Andrey Pototsky https://orcid.org/0000-0001-6139-6545;
Alexander Oron https://orcid.org/0000-0002-0383-388X;
Michael Bestehorn https://orcid.org/0000-0002-3152-8356.

Appendix A

To use the numerical continuation method (Doedel *et al.* 2007), we write the minimal surface equations (2.1)–(2.3*a,b*) as a system of nine first-order autonomous equations:

$$
\left.
\begin{aligned}
\frac{\mathrm{d}\phi_1}{\mathrm{d}s_1} &= -\frac{\sin(\phi_1)}{r_1} + \frac{\rho_1 g}{\sigma_{1g}}z_1 + \frac{2}{R_1}, \\
\frac{\mathrm{d}r_1}{\mathrm{d}s_1} &= \cos(\phi_1), \\
\frac{\mathrm{d}z_1}{\mathrm{d}s_1} &= \sin(\phi_1), \\
\frac{\mathrm{d}\phi_2}{\mathrm{d}s_2} &= -\frac{\sin(\phi_2)}{r_2} + \frac{(\rho_2 - \rho_1)g}{\sigma_{12}}z_2 + \frac{2}{R_2}, \\
\frac{\mathrm{d}r_2}{\mathrm{d}s_2} &= \cos(\phi_2), \\
\frac{\mathrm{d}z_2}{\mathrm{d}s_2} &= \sin(\phi_2), \\
\frac{\mathrm{d}h}{\mathrm{d}r} &= h', \\
\frac{\mathrm{d}h'}{\mathrm{d}r} &= (1 + h'^2)^{3/2}\left(\frac{\rho_2 g}{\sigma_{2g}}h - \frac{\rho_2 g}{\sigma_{2g}}h_0 - \frac{h'}{\tilde{r}\sqrt{1 + h'^2}}\right), \\
\frac{\mathrm{d}\tilde{r}}{\mathrm{d}r} &= 1,
\end{aligned}
\right\}
\tag{A1}
$$

The new variable $\tilde{r} = r$ is introduced to allow writing the meniscus equation as an autonomous system of first-order differential equations, where we have taken special care of (2.4) by truncating the semi-infinite interval $R \le r < \infty$ to $R \le r < R_\infty$, with a fixed upper bound of $R_\infty = 10$ cm. Equations (2.1)–(2.3*a,b*) are solved on the interval $0 \le s_1 \le S_1$ and (2.4)–(2.6*a,b*) are solved on the interval $0 \le s_2 \le S_2$. Note that the first and the fourth equations in (A1) are singular at $s_i = 0$ owing to the presence of the term $\sin(\phi_i)/r_i$. To avoid singularity we introduce the following set of fourteen regularized

922 A31-18

boundary conditions:

$$\phi_1(0) = 10^{-5},$$
$$r_1(0) = 10^{-5}R_1,$$
$$z_1(0) = 0,$$
$$r_1(S_1) = R,$$
$$\phi_2(0) = 10^{-5},$$
$$r_2(0) = 10^{-5}R_2,$$
$$z_2(0) = 0,$$
$$r_2(S_2) = R,$$
$$h'(R_\infty) = 0,$$
$$h(R) = 0,$$
$$\tilde{r}(R) = R,$$
$$0 = \sigma_{1g}\cos(\phi_1(S_1)) + \sigma_{12}\cos(\phi_2(S_2)) - \sigma_{2g}\frac{1}{\sqrt{1 + [h'(R)]^2}},$$
$$0 = \sigma_{1g}\sin(\phi_1(S_1)) - \sigma_{12}\sin(\phi_2(S_2)) + \sigma_{2g}\frac{h'(R)}{\sqrt{1 + [h'(R)]^2}},$$
$$\rho_1 g(V_1 + V_2) = \rho_2 g V_2 + \rho_2 g\pi R^2 h_0 + \sigma_{2g}2\pi R\frac{h'(R)}{\sqrt{1 + [h'(R)]^2}},$$

$$(A2)$$

where the last condition represents the balance of the vertical forces acting at the triple-phase contact line. The condition $r_i(0) = 10^{-5}R_i$ together with $\phi_1(0) = 10^{-5}$ ensure that $\sin(\phi_i)/r_i = R_i^{-1}$ at $s_i = 0$.

Finally, we add two integral conditions associated with the volumes of the pendant part V_2 and the total drop volume $V_1 + V_2$:

$$V_2 = \int_0^{S_2} \pi r_2^2 \sin(\phi_2)\,\mathrm{d}s_2,$$
$$V_1 + V_2 = \int_0^{S_1} \pi r_1^2 \sin(\phi_1)\,\mathrm{d}s_1 + \int_0^{S_2} \pi r_2^2 \sin(\phi_2)\,\mathrm{d}s_2.$$

$$(A3)$$

To be able to continue to a solution of the set of nine equations with fourteen boundary and two integral conditions one requires $14 + 2 - 9 + 1 = 8$ active continuation parameters. These are chosen to be $(S_1, S_2, R_1, R_2, R, h_0, V_2)$ with one additional principal continuation parameter, such as, for example, the gravity constant g or the total drop volume $V_1 + V_2$. The AUTO files are available on demand.

Appendix B

This section summarizes the computation of the stability function $f(g)$, from (3.11) in terms of the variables z_i, ϕ_i, r_i and $h(r)$ based on (2.1)–(2.3*a,b*). Taking the level of the

fluid bath far away from the drop as a zero level, the vertical coordinate of the centre of mass of the drop z_c can be expressed as

$$z_c = \frac{\pi}{V} \left(\int_0^{S_1} r_1^2(z_1(S_1) - h_0 - z_1) \sin(\phi_1) \, ds_1 + \int_0^{S_2} r_2^2(z_2 - h_0 - z_2(S_2)) \sin(\phi_2) \, ds_2 \right),$$
(B1)

where $V = V_1 + V_2$ is the total volume of the drop and all other variables have been introduced in § 2. After some simplification we obtain

$$z_c = \frac{V_1 z_1(S_1) - \int_0^{S_1} \pi r_1^2 z_1 \sin(\phi_1) \, ds_1 - V_2 z_2(S_2) + \int_0^{S_2} \pi r_2^2 z_2 \sin(\phi_2) \, ds_2}{V_1 + V_2} - h_0.$$
(B2)

The excess potential energy U_e from (3.3) of the fluid bath is given by the potential energy of the shaded part in figure 3, filled with fluid 2 with the negative density $-\rho_2$. Here U_e can be split into the energy of the pendant part of the drop and the energy of the remaining upper part of the shaded region in figure 3:

$$U_e = -g\rho_2 \left[\int_0^{S_2} \pi r_2^2(z_2 - h_0 - z_2(S_2)) \sin(\phi_2) \, ds_2 + \int_R^{\infty} \pi r^2(h(r) - h_0) h'(r) \, dr \right],$$
(B3)

where R is the contact radius. Finally, the stability function $f(g)$ is

$$f(g) = z_c + \frac{U_e}{gV\rho_1}.$$
(B4)

REFERENCES

APFFEL, B., NOVKOSKI, F., EDDI, A. & FORT, E. 2015 Floating under a levitating liquid. *Nature* **585**, 48–52.

BENILOV, E.S. 2016 Stability of a liquid bridge under vibration. *Phys. Rev.* E **93**, 063118.

BESTEHORN, M. & POTOTSKY, A. 2016 Faraday instability and nonlinear pattern formation of a two-layer system: a reduced model. *Phys. Rev. Fluids* **1**, 063905.

BOUCHER, E.A., EVANS, M.J.B. & FRANK, F.C. 1975 Pendent drop profiles and related capillary phenomena. *Proc. R. Soc. Lond.* A **346** (1646), 349–374.

BRATUKHIN, Y.K. & MAKAROV, S.O. 1994 *Interphase convection*. Perm University Press.

BRATUKHIN, Y.K., MAKAROV, S.O. & TEPLOVA, O.V. 2001 Equilibrium shapes and stability of floating drops. *Fluid Dyn.* **36**, 529–537.

DOEDEL, E.J., FAIRGRIEVE, T.F., SANDSTEDE, B., CHAMPNEYS, A.R., KUZNETSOV, Y.A. & WANG, X. 2007 Auto-07p: Continuation and bifurcation software for ordinary differential equations. *Tech. Rep.*

GEORGE, D., DAMODARA, S., IQBAL, R. & SEN, A.K. 2016 Flotation of denser liquid drops on lighter liquids in non-Neumann condition: role of line tension. *Langmuir* **40**, 10276–10283.

HARTLAND, S. & BURRI, J. 1976 Das maximale volumen einer linse an einer fluid-flüssig grenzfläche. *Chem. Engng J.* **11** (1), 7–17.

HARTLAND, S. & ROBINSON, J.D. 1971 The dynamic equilibrium of a rigid sphere at a deformable liquid-liquid interface. *J. Colloid Interface Sci.* **35** (3), 372–378.

LANDAU, L.D. & LIFSHITZ, E.M. 1987 *Fluid Mechanics*. Course of Theoretical Physics, vol. 6. Pergamon.

LAPUERTA, V., MANCEBO, F.J. & VEGA, J.M. 2001 Control of Rayleigh–Taylor instability by vertical vibration in large aspect ratio containers. *Phys. Rev.* E **64**, 016318.

LOHNSTEIN, T. 1906 Zur theorie des abtropfens mit besonderer rücksicht auf die bestimmung der kapillaritätskonstanten durch tropfversuche. *Ann. Phys.* **325** (7), 237–268.

NEPOMNYASHCHY, A. 2021 Droplet on a liquid substrate: wetting, dewetting, dynamics, instabilities. *Curr. Opin. Colloid Interface Sci.* **51**, 101398.

OOI, C.H., PLACKOWSKI, C., NGUYEN, A.N., VADIVELU, R.K., JOHN, J.A.S., DAO, D.V. & NGUYEN, N.-T. 2016 Floating mechanism of a small liquid marble. *Sci. Rep.* **6**, 21777.

PADDAY, J.F. & PITT, A. 1973 The stability of axisymmetric menisci. *Phil. Trans. R. Soc. Lond.* A **275**, 489–528.

PHAN, C.M. 2014 Stability of a floating water droplet on an oil surface. *Langmuir* **30** (3), 768–773.

PHAN, C.M., ALLEN, B., PETERS, L.B., LE, T.N. & TADE, M.O. 2012 Can water float on oil? *Langmuir* **28** (10), 4609–4613.

POTOTSKY, A. & BESTEHORN, M. 2016 Faraday instability of a two-layer liquid film with a free upper surface. *Phys. Rev. Fluids* **1**, 023901.

POTOTSKY, A. & BESTEHORN, M. 2018 Shaping liquid drops by vibration. *Europhys. Lett.* **121** (4), 46001.

POTOTSKY, A., MAKSYMOV, I.S., SUSLOV, S.A. & LEONTINI, J. 2020 Intermittent dynamic bursting in vertically vibrated liquid drops. *Phys. Fluids* **32** (12), 124114.

POTOTSKY, A., ORON, A. & BESTEHORN, M. 2019 Vibration-induced floatation of a heavy liquid drop on a lighter liquid film. *Phys. Fluids* **31** (8), 087101.

PRINCEN, H.M. 1963 Shape of a fluid drop at a liquid–liquid interface. *J. Colloid Sci.* **18**, 178–195.

PRINCEN, H.M. & MASON, S.G. 1965 Shape of a fluid drop at a fluid–liquid interface. I. Extension and test of two-phase theory. *J. Colloid Sci.* **20** (2), 156–172.

PUCCI, G., BEN AMAR, M. & COUDER, Y. 2013 Faraday instability in floating liquid lenses: the spontaneous mutual adaptation due to radiation pressure. *J. Fluid Mech.* **725**, 402–427.

PUCCI, G., BEN AMAR, M. & COUDER, Y. 2015 Faraday instability in floating drops. *Phys. Fluids* **27** (9), 091107.

PUCCI, G., FORT, E., BEN AMAR, M. & COUDER, Y. 2011 Mutual adaptation of a faraday instability pattern with its flexible boundaries in floating fluid drops. *Phys. Rev. Lett.* **106**, 024503.

SAHASRABUDHE, S.N., RODRIGUEZ-MARTINEZ, V., O'MEARA, M. & FARKAS, B.E. 2017 Density, viscosity, and surface tension of five vegetable oils at elevated temperatures: measurement and modeling. *Intl J. Food Prop.* **20** (sup2), 1965–1981.

SMITH, J.D., DHIMAN, R., ANAND, S., REZA-GARDUNO, E., COHEN, R.E., MCKINLEY, G.H. & VARANASI, K.K. 2013 Droplet mobility on lubricant-impregnated surfaces. *Soft Matt.* **9**, 1772–1780.

STERMAN-COHEN, E., BESTEHORN, M. & ORON, A. 2017 Rayleigh–Taylor instability in thin liquid films subjected to harmonic vibration. *Phys. Fluids* **29** (5), 052105.

WOLF, G.H. 1969 The dynamic stabilization of the Rayleigh–Taylor instability and the corresponding dynamic equilibrium. *Z. Phys.* A **227** (3), 291–300.

WOLF, G.H. 1970 Dynamic stabilization of the interchange instability of a liquid–gas interface. *Phys. Rev. Lett.* **24**, 444–446.

WONG, C.Y.H., ADDA-BEDIA, M. & VELLA, D. 2017 Non-wetting drops at liquid interfaces: from liquid marbles to leidenfrost drops. *Soft Matt.* **13**, 5250–5260.